CrystEngComm

PAPER

View Article Online
View Journal | View Issue

Check for updates

Cite this: *CrystEngComm*, 2023, **25**, 3755

A homogeneity study on $(Ce,Gd)_3Ga_2Al_3O_{12}$ crystal scintillators grown by an optical floating zone method and a traveling solvent floating zone method

Tong Wu,[ab] Ling Wang,[ab] Yun Shi, *[ac] Qian Zhang,[a] Yifei Xiong,[a] Qiang Yuan,[a] Tongtong Li,[a] Kaicheng Ma,[a] Hui Wang,[a] Jinghong Fang,[a] Jinqi Ni,[a] Huan He,[a] Zhenzhen Zhou,[a] Qian Liu,[ac] Jianding Yu[ac] and Jun Zou [d]

1 at% Ce^{3+}-doped $Gd_3Ga_2Al_3O_{12}$ (GGAG) single crystals were grown by an optical floating zone (OFZ) method and a traveling solvent floating zone (TSFZ) method. To reveal their structure and chemical composition homogeneity, X-ray diffraction (XRD) and high-resolution inductively coupled plasma atomic emission spectrometry (ICP-AES) were conducted on the as-grown Ce:GGAG crystals at 4 different positions along the growth direction. Compared with the Ce:GGAG crystals grown by the OFZ method (Ce:GGAG-OFZ), the Ce:GGAG crystals grown by the TSFZ method (Ce:GGAG-TSFZ) presented better Ce^{3+} distribution homogeneity which varied from 0.21 to 0.29 at%. However, the segregation coefficient of Ce^{3+} in Ce:GGAG-OFZ was found to be higher than that in Ce:GGAG-TSFZ, revealing a different solidification rate between them. The comparison study shows that the photoluminescence (PL) intensity of Ce:GGAG-TSFZ is about twice higher than that of Ce:GGAG-OFZ and the maximum light yield (LY) of 35 340 photons per MeV also occurs in the former. Trap depths were measured to be 0.70 eV and 0.98 eV by TL glow curves. The LY value of Ce:GGAG-TSFZ along the growth direction fluctuated to a lesser extent with respect to that of Ce:GGAG-OFZ; the latter decreases gradually along the growth direction. It is concluded that the TSFZ method helps to improve the homogeneity of crystal composition when growing crystals with multiple compositions or incongruent compounds.

Received 13th February 2023,
Accepted 24th May 2023

DOI: 10.1039/d3ce00144j

rsc.li/crystengcomm

1 Introduction

Driven by the development of radiation detectors, the core component of nuclear medicine imaging apparatus and other radiation detecting instruments, scintillators which can absorb and convert high-energy radiation (X- or γ-rays, α, β particles) to visible or ultraviolet (UV) photons have attracted worldwide research interests. Light yield (LY), decay time, energy resolution and afterglow of the scintillators are major factors.[1–4] In the past decades, bandgap engineering strategy has been successfully used to optimize scintillation performance by adjusting the bandgap energy, electron structure (*i.e.*, energy level position of activators or traps)[5–8] and the thermal ionization length of the electron–hole pair[9,10] as well. As a representative, Ce^{3+}-doped multiple aluminate garnet compounds, $(Ce,Gd)_3(Al,Ga)_5O_{12}$ (Ce:GGAG), have been proposed to be one of the promising scintillators for applications of X-ray detection, medical imaging *etc.*[11–15] The emission of Ce^{3+} in it is characterized by an electron transition from the lowest 5d ($5d_1$) energy level to the 4f energy level[16,17] which could realize both fast decay time and high LY.

By the Czochralski (CZ) method,[18–20] crack-free Ce:GAGG crystals of 2, 3 and 4 inches were grown. However, an oxygen-rich condition is desired to inhibit the decomposition of Ga_2O_3 ($Ga_2O_3 \rightarrow Ga_2O + O_2$), which occurs at high melting temperature,[21] whereas it is difficult for the CZ method because of the need to avoid iridium crucible oxidation. The contamination coming from the iridium particles that evaporate during the high melting process and the anoxic environment usually leads to the twisted growth and composition segregation of Ce:GGAG crystals, especially in compositions where the Ga/Al ratio is or lower than 2/3,[21] although higher luminescence efficiency occurs since their

---

[a] Shanghai Institute of Ceramics, Chinese Academy of Sciences, Shanghai 200050, China. E-mail: shiyun@mail.sic.ac.cn
[b] College of Physical Science and Technology, Central China Normal University, Wuhan 430079, China
[c] Center of Materials Science and Optoelectronics Engineering, University of Chinese Academy of Science, Beijing 100049, China
[d] Shanghai Institute of Technology, Shanghai, 201418, China

energy bandgap decreases with Ga content.[7] In 2019, Bartosiewicz[13] *et al.* reported that the unbalanced substitution of Ga for Al makes the garnet phase thermodynamically unstable and results in the formation of undesired secondary perovskite phases ($GdAlO_3$, GAP). Meanwhile, irregular profiles and opaque morphologies were exhibited as well as heavy segregation occurred, especially in the case of low Ga/Al ratio, which was caused by incongruent melting composition and formation of different phases during the crystal growth process.[22] To improve the lattice stability of GAG phase, partial substitution of Ln (Ln = Y, Lu, Tb) with ion radii smaller than Gd^{3+} at dodecahedral sites has been extensively studied. Light output up to 230% relative to BGO and 20–40 ns decay times were achieved at Ga concentrations of 60–75 at% in $Y_3Al_{5-x}Ga_xO_{12}$:Ce (YAGG:Ce) scintillator crystals.[23] However, components with low Ga ratios are still difficult to obtain in bulk single crystals despite successful preparation in thin films using the liquid epitaxy (LPE) growth method[24] with, unfortunately, slow decay of $t_{1/e}$ = 270–280 ns and $t_{1/20}$ = 1280–1300 ns.

Alternatively, the OFZ method was proposed in the growth of scintillation single crystals. Highly transparent $(Lu_{0.3}Gd_{0.7})_2SiO_5:Y^{3+}$ (5 at%) single crystals were obtained by a laser floating zone (LFZ) technique in air at 10 mm h^{-1};[25] the introduction of Y^{3+} increased the plasticity, thus reducing stress and therefore minimizing crack formation. Ce:GGAG crystals with low Ga/Al ratio (Ga/Al = 2/3) with a fast scintillation decay time and high ratio of the fast decay component (105 ns/80% + 349 ns/20%) were then obtained.[26] Recently, we further optimized the scintillation decay performance of the Ce:GGAG crystal (Ga/Al = 2/3) to 52 ns/48% + 122 ns/52% and the optimum scintillation LY reached 33 791 photons per MeV at 0.75 μs time gate by the OFZ method.[27] This was attributed to the oxygen-rich environment (100% O_2) during the growth process which can suppress Ga_2O_3 evaporation and formation of oxygen vacancies; the latter would act as shallow traps and degrade the luminescence efficiency and decay.[28,29] Besides the growth atmosphere, heating power and rotation rates, the shape of the molten zone and solid–liquid interface are also essential to obtain crack-free crystals with uniform composition distribution.[30,31] We explored the TSFZ method[30] to grow Ce:GGAG (Ga/Al = 2/3) crystals by using $(Gd_2O_3)_x(Al_2O_3)_{1-x}$ (x = 25, 27, 29 mol%) ceramic blocks as the traveling solvent. The optimum scintillation decay and LY value reached 64 ns/85%+ 164 ns/15%, 34 132 photons per MeV, according to the stable zone.[30]

The TSFZ method is equivalent to the FZ growth with a solvent by the zone-leveling effect of the zone-melting process.[32,33] It was widely used to grow incongruent-melting compounds and solid solutions, such as $LaCuO_2$ superconductors[34] and $La_{2/3-x}Li_{3x}TiO_3/Li_xLa_{(1-x)/3}NbO_3$ solid electrolytes.[33,35] Recently, Ce-doped $Gd_2Si_2O_7$ and ZnO:Ga crystal scintillators were also successfully grown by the TSFZ method.[36,37] However, the application of the TSFZ method in scintillation crystals is still comparatively rare.

In summary, both OFZ and TSFZ are available to grow Ce:GGAG crystals, especially for compositions with low Ga/Al ratio which are difficult to grow by traditional crystal methods, such as the CZ method, micro-pulling-down (μ-PD) method[13] *etc.* Considering the effect of segregation coefficient of Ce^{3+} ion in GGAG crystal,[27,38] the Ce^{3+} distribution in the parallel and cross-sectional region of the crystals along the growth direction should be different, it would affect the homogeneity of the scintillation performance. In addition, the uneven heat distribution in the crystal volume may induce the formation of a heterogeneous phase,[13,22] a homogeneity study on the crystals is essential. In this paper, we selected 4 positions of the crystals grown by the OFZ and TSFZ methods to elucidate the difference. In addition, different from our previous TSFZ work,[30] CeO_2 and Ga_2O_3 were added simultaneously into the solvent to investigate the compensation effect of Ce^{3+} and Ga^{3+} considering their possible evaporation loss during the crystal growth.

2 Experimental section

2.1. Crystal growth

Commercial CeO_2, Gd_2O_3, Ga_2O_3 and Al_2O_3 powders with high purity (>4 N) were used as starting raw materials and mixed according to the composition $(Ce_{0.01}Gd_{0.99})_3Ga_2Al_3O_{12}$. Then they were calcined at 1350 °C for 8 h in an air atmosphere. The resultant powders were reground and put into a balloon to form cylindrical shaped rods under a cold isostatic pressure of 70 MPa, after which the rods were sintered at 1600 °C for 8 h in an O_2 atmosphere to form feed ceramic rods with high density. Then the feed rods and seed rods were installed in a furnace for crystal growth, as shown in Fig. 1.

In addition, for the TSFZ method, the solvent block was fabricated by the same route according to the composition $Ce_{0.01}Gd_{0.99}Ga_{0.55}Al_{2.45}O_{6.015}$. The solvent rods were sintered at 1500 °C in an oxygen atmosphere for 10 hours in a tube furnace to form ceramic rods which were then cut to a dimension of around ∅ 6 mm × 3 mm. The solvent ceramic rod was put onto the seed rod for the following crystal growth, as shown in Fig. 1(b). Ce:GGAG crystal rods grown by the OFZ method in our previous work[27,30] were used as the seed rods.

Crystal growth was carried out in an optical floating zone furnace (Crystal Systems Corporation, FZ-T1000H CSC Cop., Japan) with 4 × 1 kW halogen lamps as infrared radiation sources focused by four polished elliptical mirrors. The program was set to the halogen lamp output power of 2000 W (70%) using the rise rate of 66 W min^{-1}, and then the power was manually tuned until the upper surface of the seed rod (for the OFZ method, see Fig. 1(a)) or solvent blocks (for the TSFZ method, see Fig. 1(b)) melts slightly. Then, in quick succession, the feed rod would move down to achieve an abutting joint. After a while, a stable molten zone formed between the feed rod and the seed rod. The rotation rate of the seed rod and the feed rod was 10–15 rpm, and they rotated in opposite directions to realize full stirring in the

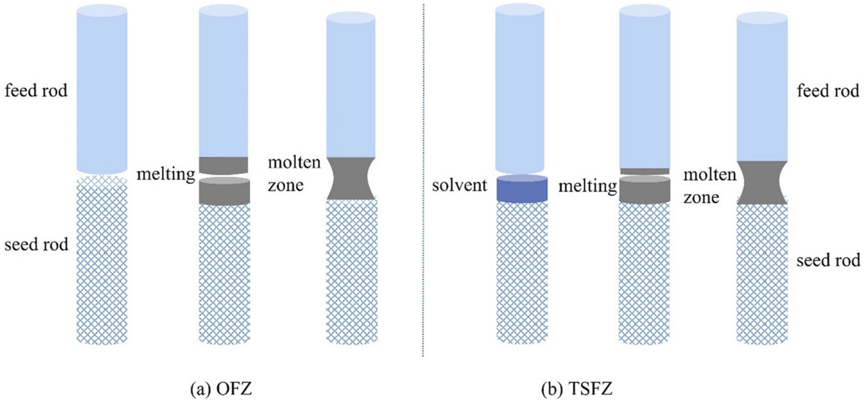

Fig. 1 Formation of molten zone established by (a) the OFZ and (b) the TSFZ method.

molten zone. The crystal growth was carried out in a 3 bar oxygen atmosphere to inhibit the volatilization of Ga_2O_3 at high temperature. The as-grown Ce:GGAG crystal rods are around 6 mm in diameter. They were cut to wafers along the growth direction for the following measurement; the interval distance between the 4 cuts is 8 mm. All crystals were double face polished to a thickness of 2 mm for absorption spectrum measurement.

2.2. Characterization

Powder X-ray diffraction (PXRD) measurement of $(Ce,Gd)_3$-$Ga_2Al_3O_{12}$ crystals was carried out in the range of 20–90° using a Rigaku Ultima IV diffractometer (Cu Kα, 40 kV, 40 mA, Rigaku Ultima IV, Japan); the baseline was subtracted using Jade software. The scanning step and rate were 0.02 and 5° min^{-1}, respectively. High-resolution inductively coupled plasma atomic emission spectrometry (ICP-AES) was performed to analyze the composition variation of the as-grown crystals along the growth direction. The absorption spectra were recorded using a Varian Cary 5000 UV-vis-NIR photometer. The photoluminescence (PL) and photoluminescence excitation (PLE) spectra were measured in a Hitachi F-4600 fluorescence spectrometer. X-ray excited luminescence (XEL) spectra were measured using a self-assembled X-ray spectrometer (X-ray tube: 70 kV, 1.5 mA).

Thermoluminescence (TL) curves were measured using a thermoluminescent dosimeter (Guangzhou Radiation Science and Technology Co. Ltd., China). The TL spectra were characterized from room temperature to 300 °C. The crystals were *in situ* radiated with UV light from a xenon lamp. The pulse height spectra were recorded by a Hamamatsu R878 photomultiplier (1 kV) using 662 keV γ-ray excitation (^{137}Cs source) as a radiation source. LY values (photons per MeV) of the as-grown Ce:GGAG crystals were calculated by comparing with a standard Ce:GGAG crystal (LY 58 000 photons per MeV, size: 27 mm × 15 mm × 2.37 mm) with a corresponding peak at 481.6 nm, FWHM 33.60, E.R. 6.98%.

3 Results and discussion

3.1. Morphology and quality of the crystals

For incongruently melting compounds, there is a significant composition difference between the solid and the crystalline melt. The solvent composition should be close to the liquidus region of the target composition to obtain sufficient molten zone volume.[39,40] Therefore, the solvent of the Al_2O_3-rich and Gd_2O_3-poor composition was used to grow 1% Ce:GGAG crystals in this work. Fig. 1 shows the schematic of the crystal growth process by the OFZ and TSFZ methods. During the growth process of the OFZ method, as shown in Fig. 1(a), both the feed rod and seed rod should be melted before junction, and then the feed rod should be quickly put down to form a joint with the seed rod. During the growth process of the TSFZ method, the solvent wafer needs to be melted first and then the upper feed rod was timely moved to stick to the solvent wafer, and in quick succession, they were pulled up together after junction (see Fig. 1(b)).

Photographs of the as-grown Ce:GGAG-OFZ and Ce:GGAG-TSFZ crystal rods are shown in Fig. 2. Ce:GGAG-OFZ presents an irregular contour while Ce:GGAG-TSFZ holds a regular shape. It is ascribed to the introduced solvent since the shape of the molten zone was continuously stabilized during the crystal growth process of the TSFZ method with respect to the OFZ method. We can also find the color difference between the as-grown Ce:GGAG-OFZ and Ce:GGAG-TSFZ, and the Ce:GGAG-OFZ rod is more opaque than that of Ce:GGAG-TSFZ (see Fig. 2(c)). It might be due to the possibly slight Ga_2O_3 evaporation of the feed rod or inhomogeneous composition distribution caused by incongruent melting in Ce:GGAG,[18] which might accordingly introduce the variation of growth rate in different directions and thus lead to unstable change of the molten zone during the OFZ method. Comparatively, the molten zone of Ce:GGAG-TSFZ can be formed at a relatively low temperature according to the use of solvent, whereas the Ga_2O_3 evaporation and incongruent melting were inhibited effectively. In addition, the stable solid–liquid interface and the high temperature gradient near the

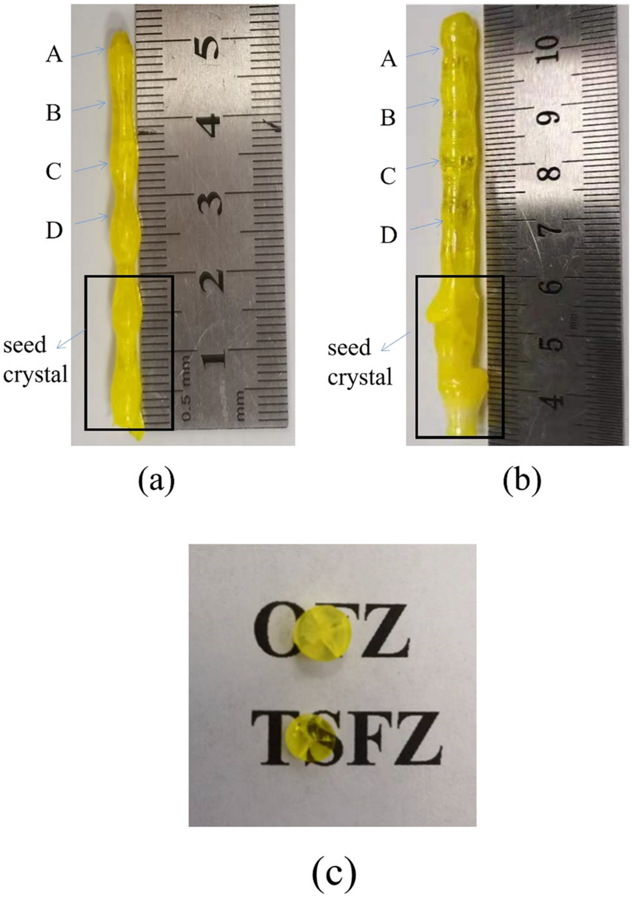

(a) (b)

(c)

Fig. 2 Photographs of the as-grown (a) Ce:GGAG-OFZ crystal rod, (b) Ce:GGAG-TSFZ crystal rod and (c) their cross section.

molten zone can maintain a higher crystallization driving force.[37,41]

3.2. Structure and composition homogeneity

For the application of crystal scintillators, it is also important to have a uniform distribution of the doping elements which will directly affect the consistency and homogeneity of their optical and luminescence performance. The segregation coefficient of the Ce^{3+} ion in GGAG crystals grown by the CZ method was reported to be $K(Ce^{3+}) = 0.36$,[38] much less than 1. The low segregation coefficient may lead to significant segregation of the dopants in the crystal growth,[36] that is, the non-uniform distribution of doped elements.[42] We investigated the composition distribution of Ce^{3+} in the as-grown Ce:GGAG-OFZ and Ce:GGAG-TSFZ crystals by ICP-AES and calculated its segregation coefficient according to the equation:

$$K_0 = C_A/C_m \tag{1}$$

where C_A is the Ce^{3+} concentration in the as-grown crystals and C_m is the Ce^{3+} concentration in the initial melt.[40] As shown in Table 1, the Ce^{3+} distribution of Ce:GGAG-TSFZ is relatively homogeneous, ranging from 0.21 at% to 0.29 at% at 4 different positions (A–D in Fig. 2) along the growth direction, whereas the homogeneity of Ce^{3+} distribution in Ce:GGAG-OFZ is comparatively worse (ranging from 0.50 at% to 0.76 at%). In addition, one can find that the calculated Ce^{3+} concentration in Ce:GGAG-OFZ was overall higher than that of Ce:GGAG-TSFZ, as shown in Table 1 and Fig. 3. It revealed a different solidification rate between the two methods although their growth rates are the same during the crystal growth process. We suspect that since the solvent would not penetrate deeply into the feed or seed rod by the capillarity action along the grain boundaries,[37] a clear and smooth solid–liquid interface could thereby be kept during the process of dissolving the feed rod in the solvent; the mass transfer rate of the diffusion layer at the solid–liquid interface is slow[43] and the exchange of Ce^{3+} between the melt of the feed and seed rod may be hindered by the clear interface of the solvent, and thus the solid solution of Ce^{3+} was limited accordingly.

Fig. 4 shows the PXRD patterns of the as-grown Ce:GGAG-OFZ and Ce:GGAG-TSFZ. Ceramic solvent with the composition $CeO_2:Gd_2O_3:Ga_2O_3:Al_2O_3 = 0.01:1:0.55:2.45$ was used in the TSFZ method. It is shown that all of the as-grown crystals are in the single cubic garnet phase compared with the standard $Gd_3Al_3Ga_2O_{12}$ diffraction pattern (PDF #46-0448) and no obvious secondary phase (*i.e.*, GAP) was observed. We calculated its lattice constant through JADE software. It was found that the crystal lattice of Ce:GGAG-TSFZ (lattice constant 12.2096 nm) shrinks compared to that of Ce:GGAG-OFZ (lattice constant 12.2286 nm), which may be

Table 1 The experimental and calculated Ce^{3+} concentrations which were obtained by ICP-AES

As-grown crystals	Different positions of crystals	Ce:GGAG-OFZ	Ce:GGAG-TSFZ
Experimental Ce (wt%) concentration by ICP-AES	A	0.24	0.13
	B	0.36	0.14
	C	0.34	0.11
	D	0.25	0.10
Calculated Ce (at%) concentration from experimental data of ICP-AES	A	0.5	0.27
	B	0.76	0.29
	C	0.71	0.23
	D	0.52	0.21
Nominal Ce (at%) concentration in crystals		1	1

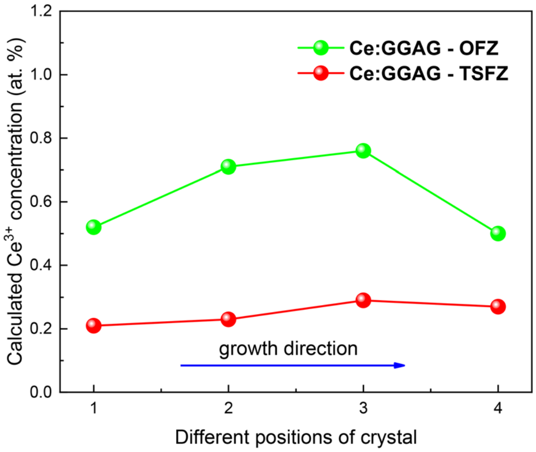

Fig. 3 The variation of Ce^{3+} concentrations along the crystal growth direction.

attributed to the relatively low concentration of Ce^{3+} retained in Ce:GGAG-TSFZ. According to the Bragg equation ($2d\sin\theta = n\lambda$), the Ce:GGAG-OFZ crystal with more Ce^{3+} ions occupied (1.14 Å, 8 coordination number) will lead to lattice expansion since its radius is larger than that of Gd^{3+} (1.05 Å, 8 coordination number).

3.3. Optical and luminescence properties

The crystal blocks at 4 different positions along the growth direction were polished to a thickness of 2 to 3 mm for measurement. The absorption spectra in the 200–800 nm range of the Ce:GGAG crystals are shown in Fig. 5. The absorption band peak around 450 nm, which belongs to the transition from the 4f ground state to the $5d_1$ excited state, is attributed to the allowed electric dipole transition between Ce^{3+} levels splitting under the crystal field. Broad absorption in the 200–350 nm region may be derived from the overlap of the Ce^{3+} $4f–5d_{2,3}$ transitions, Ce^{4+} charge transfer (CT) transition and Gd^{3+} ($8S_{7/2} \rightarrow 6I_j$, $6P_j$ transitions) related absorption.[44–46] In addition, the overall absorption difference in the 500–800 nm range is related to the diffraction or reflection caused by the light scattering sources inside the crystals, such as cracks, inclusions and or other possible defects on the atomic level. In Fig. 4(a), the transmittance in the visible light range of Ce:GGAG-OFZ in the D position is obviously low, which is consistent with its opaque appearance and visible cracks revealed by the cross section photograph in Fig. 2(c).

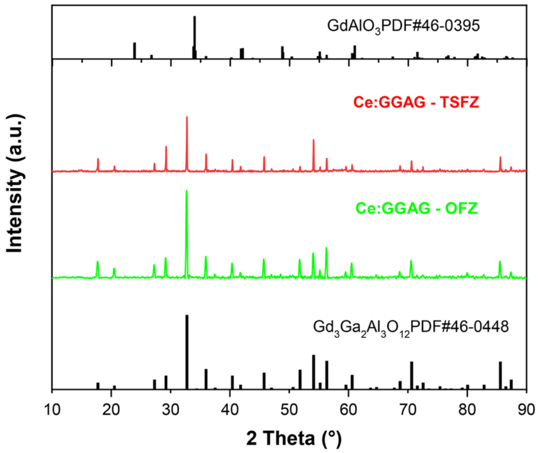

Fig. 4 PXRD patterns of the as-grown 1 at% Ce-doped GGAG single crystals. The green line represents Ce:GGAG-OFZ and red line represents Ce:GGAG-TSFZ.

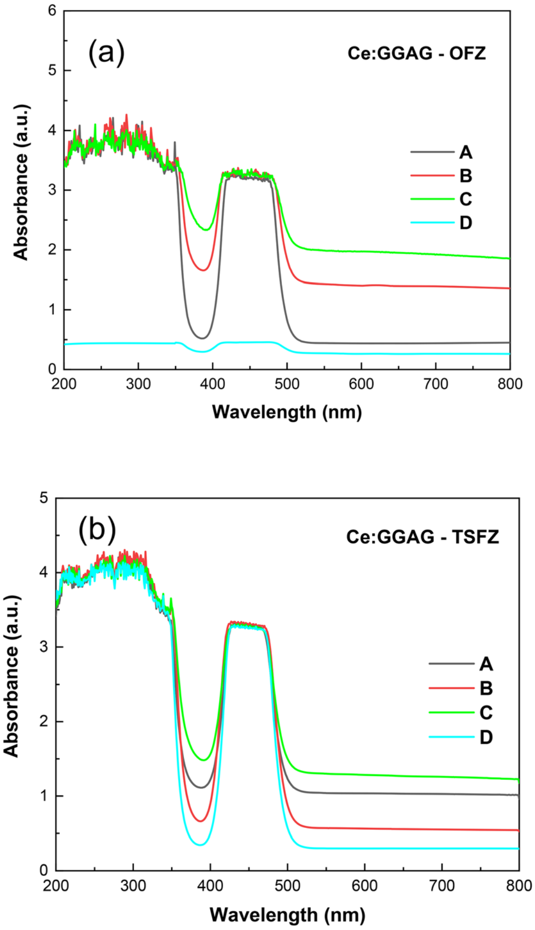

Fig. 5 Absorption spectra of (a) Ce:GGAG-OFZ and (b) Ce:GGAG-TSFZ (2 mm thickness).

The PLE and PL spectra of the Ce:GGAG-OFZ and Ce:GGAG-TSFZ crystal powders are shown in Fig. 6. Excitation between 300 and 400 nm can be observed from the PLE spectra for emission at 530 nm which corresponds to the $4f \rightarrow 5d_2$ and $4f \rightarrow 5d_1$ transition of Ce^{3+}, respectively.[45] The sharp lines observed in the 302–313 nm range are ascribed to the $8S_{7/2} \rightarrow 6I_J$ excitation transition of the Gd^{3+} ion.[15] The PL intensity of Ce:GGAG-TSFZ is about twice that of Ce:GGAG-OFZ. According to the ICP test results, the calculated Ce^{3+} concentration in the as-grown crystals ranged from 0.21 to 0.29 at% (Ce:GGAG-TSFZ, 0.08% variation scale) and 0.50 to 0.76 at% (Ce:GGAG-OFZ, 0.26% variation scale). The results are consistent with our previous study on PL intensity dependence on Ce^{3+} concentration;[27] in that study we found

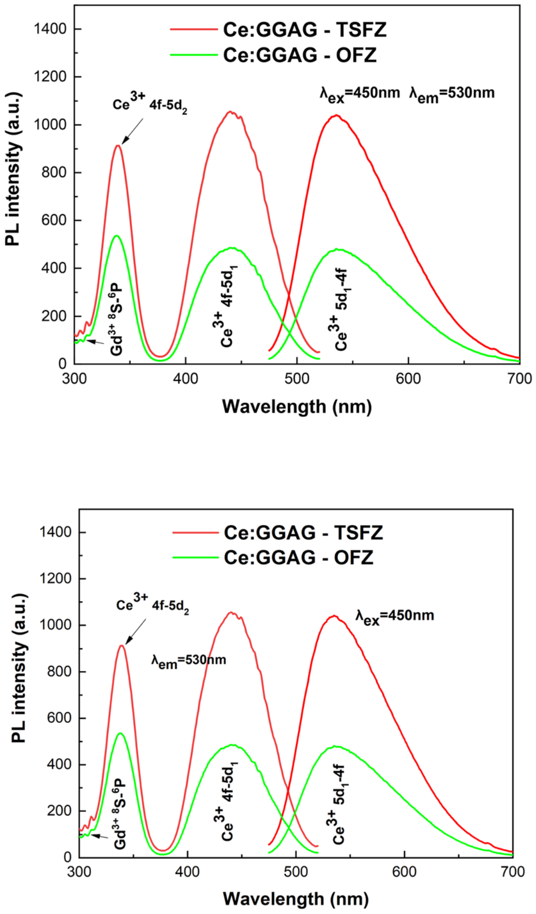

Fig. 6 PLE and PL spectra of Ce:GGAG-OFZ (green line) and Ce:GGAG-TSFZ (red line), λ_{ex} = 450 nm, λ_{em} = 530 nm.

that the PL intensity in the Ce^{3+} concentration range of 0.11–0.29 at% is higher than that of the 0.2–0.8 at% range. The difference in actual Ce^{3+} concentration between the different positions may be attributed to (1) composition deviation caused by Ce evaporation. During crystal growth, the feed rod is continuously moved down to the heating area for crystal growth. Considering that the end of the feed rod of crystal growth lasts for a long time at high temperature, the volatilization loss of Ce may be more serious than that in the early and middle stages of growth. (2) The fluctuation of Ce concentration distribution. The variation scale of Ce^{3+} concentrations in the two methods is 0.08% for the OFZ method and 0.26% for the TSFZ method; in a sense, little has changed.

Table 2 The estimated distance (R) between Ce^{3+}–Ce^{3+} ions in the GGAG crystals

As-grown crystals	The distance (R) between Ce^{3+}–Ce^{3+} ions in GGAG (Å)				Average center distance (Å)
	A	B	C	D	
Ce:GGAG-OFZ	44.12	38.37	39.25	43.55	41.32
Ce:GGAG-TSFZ	54.18	52.90	57.16	58.92	55.79

In order to clarify the concentration quenching phenomenon more clearly, we investigated the distance (R) between Ce^{3+}–Ce^{3+} ions according to the formula:[47,48]

$$R = 2\left(\frac{3V}{4\pi NX}\right)^{1/3} \tag{2}$$

where V is the volume of the unit cell, X represents the Ce^{3+} doping content and N is the number of available crystallographic sites occupied by the activator ions in the unit cell. Here we used the calculated Ce^{3+} concentrations according to the ICP-AES characterization as X in the formula. The estimated distances (R) between Ce^{3+}–Ce^{3+} ions of the Ce:GGAG-OFZ and Ce:GGAG-TSFZ are summarized in Table 2, in which we can see that the R of Ce:GGAG-TSFZ along the growth direction is overall higher than that of Ce:GGAG-OFZ. It is proposed that the exchange interaction from the non-radiative energy transfer occurs only when R is shorter than 5 Å.[48] Here, the R values summarized in Table 2 are all much longer than 5 Å, and the non-radiative energy transfer mechanism is thus dominated by the electric multipolar interaction. In addition, we also calculated the R value of our previous work.[27] We selected the nominal 0.6% Ce^{3+} concentration case which presented the optimum PL intensity, ant R is calculated to be 51.2 Å, where X = 0.32% considering the segregation coefficient in it. Then, the luminescence concentration quenching caused by energy cascade transfer between Ce^{3+}–Ce^{3+} ions is more possible to occur in Ce:GGAG-OFZ of this work since its average distance (41.32 Å) is less than 51.2 Å. Compared with Ce:GGAG-TSFZ (R = 55.79 Å) and Ce:GGAG in our precious work (R = 51.2 Å), more content of the absorbed energy would be consumed in Ce:GGAG-OFZ due to the lattice vibration and/or energy cascade transfer rather than the luminescence combination in the Ce^{3+} center.[11,48]

3.4. RL and scintillation properties

Fig. 7 shows the RL performance of Ce:GGAG-OFZ and Ce:GGAG-TSFZ at 4 different positions in the growth direction by XEL spectra. The emission at 530 nm corresponds to the 5d–4f transition of Ce^{3+} ions. An additional emission peak at 710 nm appeared in both Ce:GGAG-OFZ and Ce:GGAG-TSFZ which was also reported in previously published 0.2 at% Ce, Mg:LuAG ceramics and Ce,Eu:$Gd_3Ga_2Al_3O_{12}$ powders.[49,50] It is possibly due to the trace impurities of Cr^{3+} or Eu^{3+} introduced from the raw material. The integral XEL intensity of Ce:GGAG-OFZ at 4 different positions decreased gradually, while the trend in Ce:GGAG-TSFZ is disordered, as shown in Fig. 7(c). The detailed mechanism is considered to be related to the difference in actual Ce^{3+} concentrations in the different positions arising from the different segregation coefficients between the OFZ method and the TSFZ method as well as the different situation of point defects inside the crystals.

Scintillation conversion can be divided into three consecutive sub-processes: conversion, transport and luminescence.[51] In the sub-processes of transport, electrons and holes (eventually created excitons) migrated through the material, repeated trapping at defects. The electrons and holes stored in traps can escape at a higher temperature by getting enough energy from the lattice vibration. To understand the defect distribution and trap depth, 4 wafers cut along the growth direction were used to record the TL glow curves of the Ce:GGAG-OFZ or Ce:GGAG-TSFZ single crystals.

Table 3 Calculated trap depth of the Ce:GGAG-OFZ and Ce:GGAG-TSFZ crystals

As-grown crystals	Trap depth (eV)			
	A	B	C	D
Ce:GGAG-OFZ	0.702 0.967	0.708 0.984	0.704 0.974	0.706 0.974
Ce:GGAG-TSFZ	—	—	—	0.690

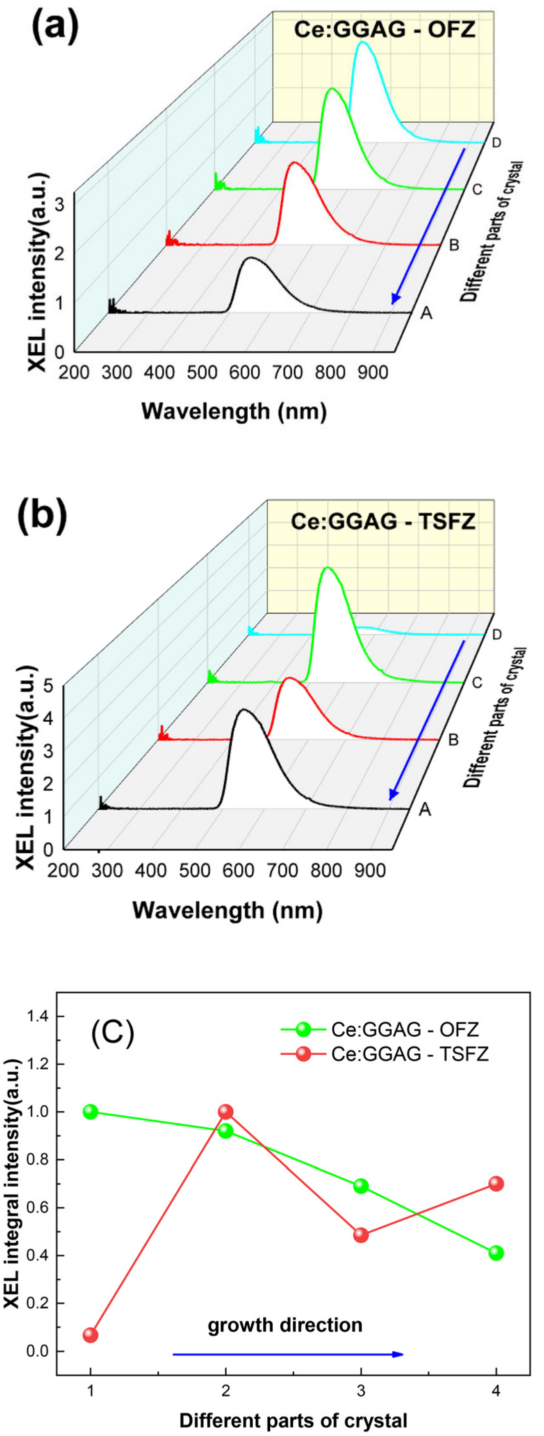

Fig. 7 XEL spectra of (a) Ce:GGAG-OFZ and (b) Ce:GGAG-TSFZ; (c) comparison of the XEL integral intensity.

The trap depths can be estimated according to Randall and Wilkins' method, as shown by eqn (3):[52,53]

$$\varepsilon = T_m/500 \tag{3}$$

where ε is the trap depth (eV) and T_m is the peak position of the TL glow curve (K). The calculated results are summarized in Table 3.

As shown in Fig. 8 and Table 3, these TL glow peaks occurred at 352 K (trap depth of 0.704 eV) and 490 K (trap depth of 0.984 eV). Meanwhile, the TL intensity of Ce:GGAG-TSFZ crystals was distinctively lower than that of Ce:GGAG-OFZ crystals, which reveals a similar defect type whereas

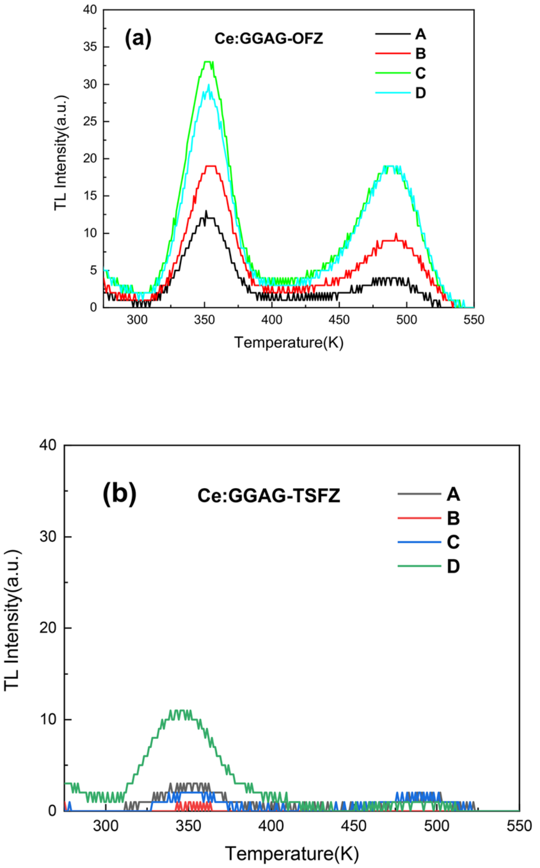

Fig. 8 TL glow curves of the (a) Ce:GGAG-OFZ and (b) Ce:GGAG-TSFZ crystals after X-ray irradiation at 77 K for 15 min; heating rate 5 K min^{-1}.

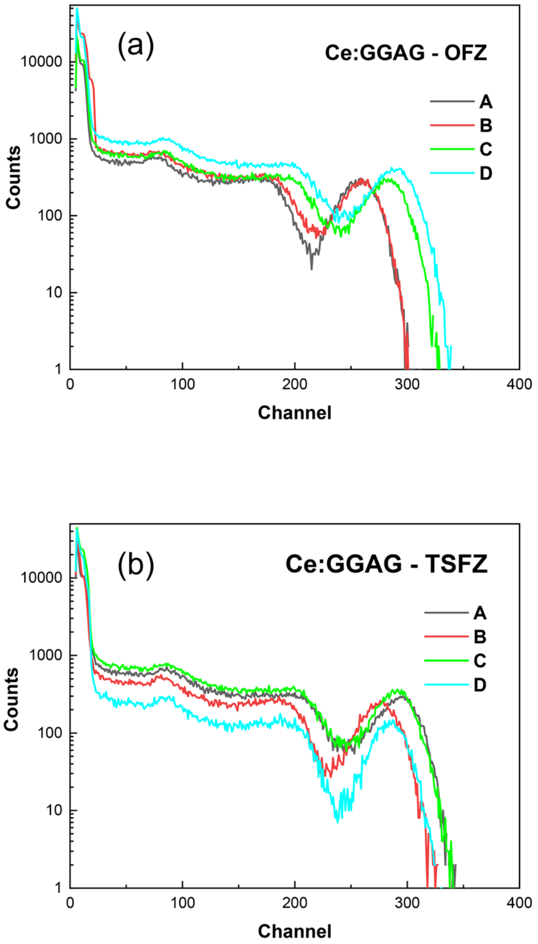

Fig. 9 Pulse height spectra of (a) Ce:GGAG-OFZ and (b) Ce:GGAG-TSFZ. The shaping time is 0.75 μs.

different defect concentration between the Ce:GGAG-TSFZ and Ce:GGAG-OFZ crystals. From the intensity of the TL glow curves, it was found that Ce:GGAG-OFZ exhibited a higher defect concentration than Ce:GGAG-TSFZ, especially for deep traps (trap depth of 0.984 eV); they can introduce energy levels into the forbidden gap and modify/degrade scintillation performance.[51] It also can help to explain the XEL intensity difference revealed in Fig. 7c. The obviously decreased TL intensity showed the advantages of the TSFZ method which exhibited lower growth temperature and stable molten zone.[27]

The pulse height spectra of the as-grown Ce:GGAG crystals were measured at room temperature under 662 keV γ-rays, as shown in Fig. 9. The results show that the LY values of Ce:GGAG-TSFZ, which were calculated by comparing with the standard Ce:GGAG crystal (LY 58 000 photons per MeV, size: 27 × 15 × 2.37 mm^3) with a corresponding peak at 481.6 nm, FWHM 33.60, E.R 6.98%, were mostly higher than that of Ce:GGAG-OFZ. As shown in Fig. 10, along the direction of crystal growth, the LY values of Ce:GGAG-OFZ and Ce:GGAG-TSFZ showed comparatively different evolution trends. Similar to the variation of XEL intensity, the LY values of Ce:GGAG-TSFZ in 4 different positions showed less variation than that of Ce:GGAG-OFZ; the latter decreased in a monodirectional way along the crystal growth direction. The results are considered to be attributable to the effect of solvent on the growth process, which can improve Ce^{3+} distribution homogeneity in the crystal.

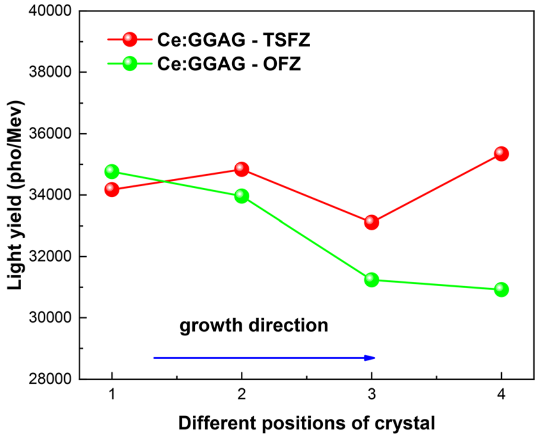

Fig. 10 The comparison of LY values of 4 different positions along the crystal growth direction of Ce:GGAG-OFZ and Ce:GGAG-TSFZ.

The concentration of Ce^{3+} in the crystals is one of the factors which would influence the scintillation light yield. As we have demonstrated in our previous work,[24] there is a quenching concentration at around nominal Ce (at%) of 0.6 at%, below which the luminescence intensity or light yield value usually increases with the Ce^{3+} concentration. However, defects inside the crystals, especially defects in atomic level, are also important factors which would influence the scintillation light yield acting as traps during the conversion, transport and luminescence process which are more complicated and unpredictable.[51] We attributed the similar light yield value in the same position of Ce:GGAG-OFZ and Ce:GGAG-TSFZ to the different defect status which compensated for their largely different Ce^{3+} concentration effect. The growth of Ce:GGAG crystal started from a 1 at% Ce^{3+} nominal concentration, while the resulting Ce^{3+} concentrations and scintillation light yield are different in Ce:GGAG-OFZ and Ce:GGAG-TSFZ, as shown in Fig. 3 and 10. It reveals a different interaction between the two methods with respect to the temperature gradient, temperature field fluctuations and environmental factors, which would lead to different status of cracks, color centers, dislocations, inclusions and scattered particles in the as-grown crystals.

4 Conclusions

A comparison study was conducted on 1 at% Ce^{3+}-doped GGAG crystal scintillators grown by the OFZ and TSFZ method. The Ce^{3+} distribution and PL and RL intensity as well as scintillation LY at 4 different positions along the crystal growth direction were investigated to elucidate the homogeneity of the crystals. The XRD patterns show that all of the as-grown crystals are in the dominant GGAG phase with a cubic garnet structure. According ICP-AES quantitative analysis, the distribution of Ce^{3+} in Ce:GGAG-TSFZ was found to be more homogeneous (0.08% variation scale) than that of Ce:GGAG-OFZ (0.26% variation scale). The main PL and RL emissions of Ce:GGAG were observed to peak at 540 nm which corresponds to 5d–4f transition of Ce^{3+} ions. Meanwhile, the PL intensity of Ce:GGAG-TSFZ is higher than that of Ce:GGAG-OFZ. Additionally, the TL glow curves revealed the existence of defects with trap depths of 0.70 eV and 0.98 eV. The LY value of Ce:GGAG-TSFZ in the 4 different parts fluctuates in a small range and the maximum LY reached 35 340 photons per MeV which is higher than that of Ce:GGAG-OFZ (34 760 photons per MeV). The superior performance of Ce:GGAG-TSFZ with respect to Ce:GGAG-OFZ was ascribed to the stable molten zone realized by the travelling solvent. The stable growth achieved by the TSFZ method is also suspected to be able to increase the extent of Ce^{3+} segregation and the incongruent melting with respect to the OFZ method and thus lead to a significant improvement of the crystal composition homogeneity. The mechanism of the PL intensity and LY value difference between Ce:GGAG-OFZ and Ce:GGAG-TSFZ was ascribed to the difference in actual Ce^{3+} concentrations in the as-grown crystals introduced by different Ce^{3+} segregation coefficients. The results show that the TSFZ method could be a more competitive way to grow Ce:GGAG crystals with low Ga/Al ratio or other crystal scintillators whose melt is incongruent.

Conflicts of interest

There are no conflicts to declare.

Acknowledgements

The authors are thankful for the financial support by the National Natural Science Foundation of China (No. 62175249), the Research Program of Shanghai Sciences and Technology Commission Foundation (No. 22511100300, 23DZ2201500) and the Strategic Priority Research Program of the Chinese Academy of Sciences (XDA22010301).

References

1. M. J. Weber, Inorganic scintillators: today and tomorrow, *J. Lumin.*, 2002, **100**, 35–45.
2. M. Nikl and A. Yoshikawa, Recent R&D Trends in Inorganic Single-Crystal Scintillator Materials for Radiation Detection, *Adv. Opt. Mater.*, 2015, **3**(4), 463–481.
3. P. Buechele, M. Richter, S. F. Tedde, G. J. Matt, G. N. Ankah, R. Fischer, M. Biele, W. Metzger, S. Lilliu, O. Bikondoa, J. E. Macdonald, C. J. Brabec, T. Kraus, U. Lemmer and O. Schmidt, X-ray imaging with scintillator-sensitized hybrid organic photodetectors, *Nat. Photonics*, 2015, **9**(12), 843–848.
4. T. M. Shaffer, C. M. Drain and J. Grimm, Optical Imaging of Ionizing Radiation from Clinical Sources, *J. Nucl. Med.*, 2016, **57**(11), 1661–1666.
5. A. Markovskyi, W. Gieszczyk, P. Bilski, A. Fedorov, K. Bartosiewicz, K. Paprocki, T. Zorenko and Y. Zorenko, Composition engineering of $Tb_{3-x}GdxAl_{5-y}Ga_yO_{12}$:Ce single crystals and their luminescent, scintillation and photoconversion properties, *J. Alloys Compd.*, 2020, **849**, 155808.
6. T. Zorenko, V. Gorbenko, S. Witkiewicz-Lukaszek and Y. Zorenko, Luminescent properties of $(La,Lu,Gd)_3(Al,Sc,Ga)_5O_{12}$:Ce mixed garnets under synchrotron radiation excitation, *J. Lumin.*, 2018, **199**, 483–487.
7. K. Kamada, T. Endo, K. Tsutumi, T. Yanagida, Y. Fujimoto, A. Fukabori, A. Yoshikawa, J. Pejchal and M. Nikl, Composition Engineering in Cerium-Doped $(Lu,Gd)_3(Ga,Al)_5O_{12}$ Single-Crystal Scintillators, *Cryst. Growth Des.*, 2011, **11**(10), 4484–4490.
8. M. Fasoli, A. Vedda, M. Nikl, C. Jiang, B. P. Uberuaga, D. A. Andersson, K. J. McClellan and C. R. Stanek, Band-gap engineering for removing shallow traps in rare-earth $Lu_3Al_5O_{12}$ garnet scintillators using Ga^{3+} doping, *Phys. Rev. B: Condens. Matter Mater. Phys.*, 2011, **84**, 081102.
9. A. V. Gektin, A. N. Belsky and A. N. Vasil'ev, Scintillation Efficiency Improvement by Mixed Crystal Use, *IEEE Trans. Nucl. Sci.*, 2014, **61**(1), 262–270.
10. O. Sidletskiy, A. Belsky, A. Gektin, S. Neicheva, D. Kurtsev, V. Kononets, C. Dujardin, K. Lebbou, O. Zelenskaya, V. Tarasov, K. Belikov and B. Grinyov, Structure-Property Correlations in a Ce-Doped $(Lu,Gd)_2SiO_5$:Ce Scintillator, *Cryst. Growth Des.*, 2012, **12**(9), 4411–4416.
11. I. Gerasymov, T. Nepokupnaya, A. Boyarintsev, O. Sidletskiy and S. Tretyak, GAGG:Ce composite scintillator for X-ray imaging, *Opt. Mater.*, 2020, **109**, 110305.
12. L. Lu, M. Sun, Q. Lu, T. Wu and B. Huang, High energy X-ray radiation sensitive scintillating materials for medical imaging, cancer diagnosis and therapy, *Nano Energy*, 2021, **79**(1), 105437.
13. K. Bartosiewicz, V. Babin, K. Kamada, A. Yoshikawa, S. Kurosawa, A. Beitlerova, R. Kucerkova, M. Nikl and Y. Zorenko, Ga for Al substitution effects on the garnet phase stability and luminescence properties of $Gd_3GaxAl_{5-x}O_{12}$:Ce single crystals, *J. Lumin.*, 2019, **216**, 116724.
14. Y. Boyarintseva, S. Neicheva, P. Zhmurin, P. Arhipov, I. Gerasymov, S. Tkachenko, O. Sidletskiy, V. Baumer, O. Vovk and S. Nizhankovskyi, Optical study of $Y_{3-x}GdxAl_5O_{12}$:Ce crystals grown from the melt, *Opt. Mater.*, 2019, **96**, 109283.1–109283.5.
15. M. Kučera, M. Nikl, M. Hanuš and Z. Onderišinová, Gd^{3+} to Ce^{3+} energy transfer in multi-component GdLuAG and GdYAG garnet scintillators, *Phys. Status Solidi RRL*, 2013, **7**(8), 571–574.
16. G. Dantelle, G. Boulon, Y. Guyot, D. Testemale, M. Guzik, S. Kurosawa, K. Kamada and A. Yoshikawa, Research on Efficient Fast Scintillators: Evidence and X-Ray Absorption Near Edge Spectroscopy Characterization of Ce^{4+} in Ce^{3+}, Mg^{2+}-co-Doped $Gd_3Al_2Ga_3O_{12}$ Garnet Crystal, *Phys. Status Solidi B*, 2020, **257**, 1900510.

17 A. Satoh, N. Kitaura, K. Kamada, A. Ohnishi, M. Sasaki and K. Hara, Time-resolved photoluminescence spectroscopy of Ce:$Gd_3Al_2Ga_3O_{12}$ crystals, *Jpn. J. Appl. Phys.*, 2014, **53**(5S1), 89–100.

18 K. Kamada, S. Kurosawa, P. Prusa, M. Nikl, V. V. Kochurikhin, T. Endo, K. Tsutumi, H. Sato, Y. Yokota and K. Sugiyama, Cz grown 2-in. size Ce:$Gd_3(Al,Ga)_5O_{12}$ single crystal; relationship between Al, Ga site occupancy and scintillation properties, *Opt. Mater.*, 2014, **36**(12), 1942–1945.

19 K. Kamada, Y. Shoji, V. V. Kochurikhin, S. Okumura, S. Yamamoto, A. Nagura, J. Y. Yeom, S. Kurosawa, Y. Yokota, Y. Ohashi, M. Nikl and A. Yoshikawa, Growth and scintillation properties of 3 in. diameter Ce doped $Gd_3Ga_3Al_2O_{12}$ scintillation single crystal, *J. Cryst. Growth*, 2016, **452**, 81–84.

20 V. Kochurikhin, K. Kamada, K. Jin Kim, M. Ivanov, L. Gushchina, Y. Shoji, M. Yoshino and A. Yoshikawa, Czochralski growth of 4-inch diameter Ce:$Gd_3Al_2Ga_3O_{12}$ single crystals for scintillator applications, *J. Cryst. Growth*, 2020, **531**, 125384.

21 M. Meng, Q. Qi, D. Z. Ding, C. J. He, S. W. Zhao, B. Wan, L. Chen, J. J. Shi and G. H. Ren, Twisted Growth, Component Segregation and Characteristics of $Gd_3(Al,Ga)_5O_{12}$:Ce Scintillation Crystal, *J. Inorg. Mater.*, 2021, **36**(2), 188–196.

22 S. Lakiza, O. Fabrichnaya, C. Wang, M. Zinkevich and F. Aldinger, Phase diagram of the ZrO_2–Gd_2O_3–Al_2O_3 system - ScienceDirect, *J. Eur. Ceram. Soc.*, 2006, **26**(3), 233–246.

23 O. Sidletskiy, I. Gerasymov, D. Kurtsev, V. Kononets, V. Pedash, O. Zelenskaya, V. Tarasov, A. Gektin, B. Grinyov, K. Lebbou, E. Auffray, V. Dormenev, A. Borisevich and M. Korjik, Engineering of bulk and fiber-shaped YAGG:Ce scintillator crystals, *CrystEngComm*, 2017, **19**(6), 1001–1007.

24 S. Witkiewicz-Lukaszek, V. Gorbenko, T. Zorenko, K. Paprocki, O. Sidletskiy, A. Fedorov, R. Kucerkova, J. A. Mares, M. Nikl and Y. Zorenko, Epitaxial growth of composite scintillators based on $Tb_3Al_5O_{12}$: Ce single crystalline films and $Gd_3Al_{2.5}Ga_{2.5}O_{12}$: Ce crystal substrates, *CrystEngComm*, 2018, **20**(28), 3994–4002.

25 F. Rey-García, J. Rodrigues, A. J. S. Fernandes, M. R. Soares, T. Monteiro and F. M. Costa, $(Lu_{0.3}Gd_{0.7})_2SiO_5$:$Y^{3+}$ single crystals grown by the laser floating zone method: structural and optical studies, *CrystEngComm*, 2018, **20**(45), 7386–7394.

26 A. Yoshikawa, Y. Fujimoto, A. Yamaji, S. Kurosawa, J. Pejchal, M. Sugiyama, S. Wakahara, Y. Futami, Y. Yokota and K. Kamada, Crystal growth and characterization of Ce: $Gd_3(Ga,Al)_5O_{12}$ single crystal using floating zone method in different O_2 partial pressure, *Opt. Mater.*, 2013, **35**(11), 1882–1886.

27 T. Wu, L. Wang, Y. Yun Shi, T. Z. Xu, H. Wang, J. H. Fang, J. Q. Ni, H. He, C. Y. Wang, B. Wan, D. Z. Ding, Z. Z. Zhou, Q. Liu, Q. Li, J. D. Yu, X. T. Huang, O. Shichalin and E. K. Papynov, Fast $(Ce,Gd)_3Ga_2Al_3O_{12}$ Scintillators Grown by the Optical Floating Zone Method, *Cryst. Growth Des.*, 2021, **22**(1), 180–190.

28 A. Suzuki, S. Kurosawa, J. Pejchal, V. Babin, Y. Fujimoto, A. Yamaji, M. Seki, Y. Futami, Y. Yokota and K. Yubuta, The effect of different oxidative growth conditions on the scintillation properties of Ce:$Gd_3Al_3Ga_2O_{12}$crystal, *Phys. Status Solidi C*, 2012, **9**(12), 2251–2254.

29 S. M. Koohpayeh, D. Fort, A. I. Bevan, A. J. Williams and J. S. Abell, Study of ferromagnetism in Co-doped rutile powders and float-zone grown single crystals, *J. Magn. Magn. Mater.*, 2008, **320**(6), 887–894.

30 T. Wu, L. Wang, Y. Shi, X. T. Huang, T. Z. Xu, H. Wang, J. H. Fang, J. Q. Ni, H. He, C. Y. Wang, Z. Z. Zhou, Q. Liu, B. Wan, Q. Li, J. D. Yu, M. Yang, H. Y. Li, Y. T. Wu, O. Shichalin and E. K. Papynov, Stable growth of $(Ce,Gd)_3Ga_2Al_3O_{12}$ crystal scintillators by the traveling solvent floating zone method, *CrystEngComm*, 2022, **24**(11), 2050–2056.

31 M. Higuchi and K. Kodaira, Solid-Liquid Interface Shapes in the Floating-Zone Growth of Rutile Single-Crystals, *Mater. Res. Bull.*, 1994, **29**(5), 545–550.

32 W. G. Pfann, Principles of Zone-Melting, *J. Met.*, 1952, **4**(7), 747–753.

33 Y. Maruyama, S. Minamimure, C. Kobayashi, M. Nagao, S. Watauchi and I. Tanaka, Crystal growth of $La_{2/3-x}Li_{3x}TiO_3$ by the TSFZ method, *R. Soc. Open Sci.*, 2018, **5**(12), 181445.

34 A. Mohan, B. Buchner, S. Wurmehl and C. Hess, Growth of single crystalline delafossite LaCuO2 by the travelling-solvent floating zone method, *J. Cryst. Growth*, 2014, **402**, 304–307.

35 M. S. Ali, N. Sato, I. Fukasawa, Y. Maruyama, M. Nagao, S. Watauchi and I. Tanaka, Crystal Growth and Characterization of LixLa(1-x)/3NbO3 by the Traveling Solvent Floating Zone Method, *Cryst. Growth Des.*, 2019, **19**(11), 6291–6295.

36 S. Watauchi, K. Matsuya, M. Nagao, I. Tanaka, S. Kurosawa, Y. Yokota and A. Yoshikawa, Control of the solid-liquid interface during growth of a Ce-doped $Gd_2Si_2O_7$ crystal by the traveling solvent floating zone method, *J. Cryst. Growth*, 2017, **468**, 465–468.

37 Y. F. Ma, Y. Zeng, D. Perrodin, E. Bourret and Y. J. Jiang, Single-Crystal Growth of ZnO:Ga by the Traveling-Solvent Floating Zone Method, *Cryst. Growth Des.*, 2017, **17**(3), 1008–1015.

38 K. Kamada, T. Yanagida, J. Pejchal, M. Nikl, T. Endo, K. Tsutsumi, Y. Fujimoto, A. Fukabori and A. Yoshikawa, Crystal Growth and Scintillation Properties of Ce Doped $Gd_3(Ga, Al)_5O_{12}$ Single Crystals, *IEEE Trans. Nucl. Sci.*, 2012, **59**(5), 2112–2115.

39 A. Revcolevschi and J. Jegoudez, Growth of large high-Tc single crystals by the floating zone method: A review, *Prog. Mater. Sci.*, 1997, **42**(1–4), 321–339.

40 G. J. Zhao, X. H. Zeng, J. Xu, Y. Q. Xu and Y. Z. Zhou, Characteristics of large-sized Ce: YAG scintillation crystal grown by temperature gradient technique, *J. Cryst. Growth*, 2003, **253**(1–4), 290–296.

41 R. Parvin, Y. Maruyama, M. Nagao, S. Watauchi and I. Tanaka, Effects of the Mirror Tilt Angle on the Growth of $LiCoO_2$ Single Crystals by the Traveling Solvent Floating Zone (TSFZ) Technique Using a Tilting-Mirror-type Image Furnace, *Cryst. Growth Des.*, 2020, **20**(5), 3413–3416.

42 H. Ogino, A. Yoshikawa, M. Nikl, A. Krasnikov, K. Kamada and T. Fukuda, Growth and scintillation properties of Pr-doped $Lu_3Al_5O_{12}$ crystals, *J. Cryst. Growth*, 2006, **287**(2), 335–338.

43 H. D. A. Dabkowski, Crystal Growth of Oxides by Optical Floating Zone Technique, *Handbook of Crystal Growth*, Springer, 2010, pp. 367–391.

44 L. Trinkler, B. Berzina, D. Jakimovica, J. Grabis and I. Steins, UV-light induced luminescence processes in Al_2O_3 bulk and nanosize powders, *Opt. Mater.*, 2010, **32**(8), 789–795.

45 K. Bartosiewicz, V. Babin, K. Kamada, A. Yoshikawa, J. A. Mares, A. Beitlerova and M. Nikl, Luminescence quenching and scintillation response in the Ce^{3+} doped $Gd_xY_{3-x}Al_5O_{12}$ (x=0.75, 1, 1.25, 1.5, 1.75, 2) single crystals, *Opt. Mater.*, 2017, **63**, 134–142.

46 S. P. Liu, X. Q. Feng, Z. W. Zhou, M. Nikl, Y. Shi and Y. B. Pan, Effect of Mg^{2+} co-doping on the scintillation performance of LuAG: Ce ceramics, *Phys. Status Solidi RRL*, 2014, **8**(1), 105–109.

47 G. Blasse, Energy Transfer between Inequivalent Eu^{2+} Ions, *J. Solid State Chem.*, 1986, **62**, 207–211.

48 G. Peng, Z. Zou, J. Li, J. Liao and H. Wen, $(Gd_{1-x}Tb_x)_3(Al_{1-y}Ga_y)_5O_{12}$ green phosphors with high quantum yield and low thermal quenching via modulation the Ga^{3+} admixture, *J. Lumin.*, 2021, **236**, 118066.

49 A. Yoshikawa, K. Kamada, S. Kurosawa, Y. Shoji, Y. Yokota, V. I. Chani and M. Nikl, Crystal growth and scintillation properties of multi-component oxide single crystals: Ce: GGAG and Ce:La-GPS, *J. Lumin.*, 2016, **169**, 387–393.

50 J. Barta, V. Cuba, V. Jary, A. Beitlerova, D. Panek, T. Parkman and M. Nikl, Photoinduced Preparation of Bandgap-Engineered Garnet Powders, *IEEE Trans. Nucl. Sci.*, 2018, **65**(8), 2184–2190.

51 M. Nikl, Scintillation detectors for X-rays, *Meas. Sci. Technol.*, 2006, **17**(4), R37–R54.

52 D. Zhou, Z. Wang, Z. Song, F. Wang and Q. Liu, Enhanced Persistence Properties through Modifying the Trap Depth and Density in $Y_3Al_2Ga_3O_{12}$:Ce^{3+},Yb^{3+} Phosphor by Co-doping B^{3+}, *Inorg. Chem.*, 2019, **58**(2), 1684–1689.

53 J. T. Randall and M. H. F. Wilkins, Phosphorescence and electron traps-I. The study of trap distributions, *Proc. R. Soc. London, Ser. A*, 1945, **184**(999), 365–389.